

## Article

# Sorption of Mercury in Batch and Fixed-Bed Column System on Hydrochar Obtained from Apple Pomace

Krzysztof Szostak , Gabriela Hodacka, Olga Długosz, Jolanta Pulit-Prociak and Marcin Banach \* 

Faculty of Chemical Engineering and Technology, Cracow University of Technology, 31-155 Cracow, Poland

\* Correspondence: marcin.banach@pk.edu.pl; Tel.: +48-12-628-2861

**Abstract:** This paper presents the methodology for the preparation of hydrochar obtained from waste materials of natural origin and investigates its applicability for removing mercury ions from aqueous systems. The sorption properties of the obtained hydrochar were investigated in a batch and in a flow-through column system. The hydrochar material was obtained from apple pomace, which was hydrothermally carbonized in 230 °C for 5 h in a hydrothermal reactor. The hydrochar formed in the process was thermally activated with an inert gas flow—CO<sub>2</sub>. Obtained materials were characterised with XRD, FTIR-ATR, SEM-EDS and nitrogen sorption (BET) analyses, which confirmed the obtaining of a highly porous carbon material with a specific surface area of 145.72 m<sup>2</sup>/g and an average pore diameter of 1.93 nm. The obtained hydrochar was analysed for sorption of mercury ions from aqueous solutions. Equilibrium isotherms (Langmuir, Freundlich, Dubinin–Radushkevich, Temkin, Hill, Redlich–Peterson, Sips and Toth) and kinetic models (pseudo-first order, pseudo-second order, Elovich and intraparticle diffusion) were determined. The sorption process of mercury on the obtained material is best described using the Freundlich isotherm and a pseudo-second-order kinetic model. This indicates that the process is chemical in nature. The sorption of mercury ions from an aqueous solution with a concentration of C<sub>0</sub> = 100 mg Hg/dm<sup>3</sup> has been also carried out in a flow-through column system. The data obtained from adsorption were fitted to mathematical dynamic models (Bohart–Adams, Thomas, Yoon–Nelson, Clark, BDST and Yan) to illustrate the bed breakthrough curves and to determine the characteristic column parameters. The Yan model has the best fit across the study area, although the Thomas model better predicts the maximum capacity of the bed, which is q<sub>max</sub> = 111.5 mg/g.

**Keywords:** mercury; hydrochar; sorption; column sorption system; waste materials



**Citation:** Szostak, K.; Hodacka, G.; Długosz, O.; Pulit-Prociak, J.; Banach, M. Sorption of Mercury in Batch and Fixed-Bed Column System on Hydrochar Obtained from Apple Pomace. *Processes* **2022**, *10*, 2114. <https://doi.org/10.3390/pr10102114>

Academic Editor: María Victoria López Ramón

Received: 16 September 2022

Accepted: 14 October 2022

Published: 18 October 2022

**Publisher's Note:** MDPI stays neutral with regard to jurisdictional claims in published maps and institutional affiliations.



**Copyright:** © 2022 by the authors. Licensee MDPI, Basel, Switzerland. This article is an open access article distributed under the terms and conditions of the Creative Commons Attribution (CC BY) license (<https://creativecommons.org/licenses/by/4.0/>).

## 1. Introduction

Mercury (Hg) is a chemical element that belongs to the transition metal group. It is the only element that occurs in the liquid state under normal conditions. Initially, this element, due to the lack of knowledge of its toxicity, was used as an ingredient in many products, e.g., cosmetics, paints, and medicines [1–3]. Despite its many beneficial properties, it has one major drawback which is its toxicity, which makes it impossible to use it in everyday life. Since the 1970s, the recorded production of mercury has been reduced by almost an order of magnitude to reach approximately 2000 t in the year 2000 [4]. The event that triggered the introduction of all restrictions on emissions of mercury compounds into the aquatic ecosystem, air and soil was the poisoning of the population of Minamata in Japan in the 1950s [5]. The poisoning was caused by the consumption of fish, which accumulated a particularly dangerous form of mercury—methylmercury—through environmental pollution caused by industrial waste. Exposure to mercury was considered as a major public health problem by the World Health Organization in 2007 and was updated in 2021, which means that is still relevant [6,7]. The speciation of mercury in the environment results in its global dissemination, which involves alternate reactions of oxidation and reduction [8]. The main sources of toxic mercury emissions to the environment are considered to be

solid fuel combustion, coal mining and traditional mining. Hg is taken up by roots from contaminated soils and then is transferred to the stem and leaves, finally entering into the food chain, resulting in potential health and ecological risks [9]. Therefore, it is necessary to carry out research aimed at reducing mercury emissions to the environment and to develop methods for its effective removal.

The adsorption process is one of the most important, facile, convenient, and practical technologies among the methods to remove Hg from wastewater and flue gas [10]. Several carbonaceous adsorbents, such as biochar, activated carbon, and graphene oxide [11], as well as banana peels [12], egg-shells nanoparticles [13], magnetite ( $\text{Fe}_3\text{O}_4$ ) [14] and molybdenum disulphide ( $\text{MoS}_2$ ) [15] have been used for the efficient removal of Hg.

Hydrochar, due to its highly developed porous internal structure and the presence of numerous functional groups due to the activation process, is a good candidate for usage as a sorption material. Hydrochar is obtained in the hydrothermal carbonization process, which is based on the conversion of biomass into solid carbon. Hydrochar has been successfully produced from pinewood [16], rice husk [17], pig manure [18] and food wastes (egg-shell, fish residue, breadcrumb, cooked rice) [19].

This work presents a method for obtaining hydrochar from waste materials of natural origin and the potential use of this material for the elimination of mercury ions from aqueous solutions. Determination of sorption parameters in a batch and flow-through fixed-bed column system is also presented.

## 2. Materials and Methods

### 2.1. Materials

The hydrochar was obtained from the pomace formed during the pressing of apple juice on a slow-speed juicer. Mercury(II) chloride solutions  $\text{HgCl}_2$  (Sigma-Aldrich,  $\geq 99.5\%$ ) were used as a source of mercury ions. Deionized water was used in the study.

### 2.2. Methods

#### 2.2.1. Preparation of Hydrochar

The apple pomace produced by squeezing the juice in a slow-speed juicer was dried for 24 h at  $105\text{ }^\circ\text{C}$ . The dried apple pomace was ground. To obtain hydrochar, 40 g of ground pomace and  $350\text{ cm}^3$  of deionized water were placed in a hydrothermal reactor. The carbonization process was carried out at  $230\text{ }^\circ\text{C}$  for 5 h at a fixed pressure of 27.5 bar. After the process, the obtained material was filtered and dried at  $80\text{ }^\circ\text{C}$  for 12 h. The obtained hydrochar was subjected to thermal activation at  $800\text{ }^\circ\text{C}$  for 3 h at an inert gas flow rate of  $5\text{ dm}^3\text{ CO}_2/\text{min}$ .

#### 2.2.2. Spectrophotometric Determination of Mercury Concentration

Mercury ions' concentrations were determined by a spectrophotometric method using the standard curve technique. For this purpose, an appropriate amount of  $100\text{ mg}/\text{dm}^3$  mercury standard solution was added to  $10\text{ cm}^3$  volumetric flasks so that the mercury concentrations in the flasks were respectively: 0.1, 0.2, 0.3, 0.5, 1.0, 2.0, 4.0, 4.5 and  $5.0\text{ mg}/\text{dm}^3$ . Then,  $5\text{ cm}^3$  of  $0.6\text{ mol}/\text{dm}^3$  SDS solution,  $1\text{ cm}^3$  of  $1\text{ mol}/\text{dm}^3$   $\text{H}_2\text{SO}_4$  solution and  $2\text{ cm}^3$  of  $0.01\text{ mol}/\text{dm}^3$  dithizone solution (in ethanol) were added to the flasks. Then, all of them were topped up with deionized water to the calibration line and mixed thoroughly. The solutions thus prepared were examined on a spectrophotometer at 490 nm, and a prepared blank containing deionized water instead of mercury solution was used as a reference solution. A calibration curve was plotted over the given concentration range ( $R^2 = 0.9982$ ).

#### 2.2.3. Instrumental Analysis

The concentration of mercury was determined spectrophotometrically using a Rayleigh UV-1800. The analysis of the concentrations of Hg ions before and after the sorption process allowed for determining the sorption efficiency and equilibrium sorption capacity of the obtained materials. The surface structure of the materials obtained has been analysed using

an SEM technique with EDS analyser (Vegall-TescanCompany). Phase composition of the materials was determined by X-ray diffraction (XRD) analysis in the range  $10\text{--}60^\circ 2\theta$  (Philips X'Pert camera with monochromator PW 1752/00 CuK $\alpha$ ). The Fourier Transform Infrared Radiation with Attenuated Total Reflectance (FTIR-ATR) method allowed the detection of functional groups present in the obtained sorption materials. Measurements were carried out in the range  $4000\text{--}400\text{ cm}^{-1}$  (IRSpirit Shimadzu). Specific surface area, pore size, shape and pore size distribution were determined by low-temperature nitrogen vapor sorption using the BET technique (Micromeritics ASAP2010).

Kinetics models and adsorption isotherm models in batch and flow systems were fitted to experimental data of the Hg(II) adsorption process using Matlab R2015a.

#### 2.2.4. Sorption in Batch System

For the obtained hydrochar, the sorption parameters were studied by a batch process. The process was carried out in room temperature with 50 mg of solid material and  $20\text{ cm}^3$  of mercury solution. To determine equilibrium parameters, the sorption process was carried out with solutions of 50, 75 and  $100\text{ mg Hg/dm}^3$  for 60 min, while to determine kinetic parameters, the sorption process was carried out with a solution of  $100\text{ mg Hg/dm}^3$  for 2, 5, 10, 15, 20, 30 and 60 min. After the set time, the suspensions were filtered and the mercury concentration in the filtrates was analysed. All tests were performed in triplicate. In order to determine the model best describing the sorption equilibrium, the coefficients of determination— $R^2$  and the root mean square error— $RMSE$  were compared. The model with the  $R^2$  value closest to 1 and the smallest  $RMSE$  error was referred to as the model with the best fit.

#### Sorption Equilibrium

Based on the results obtained, the sorption capacities after time  $t$  ( $q_t$ ) and in equilibrium ( $q_e$ ) were determined according to the following formulas:

$$q_t = \frac{(C_0 - C_t)}{m} \cdot V \quad (1)$$

$$q_e = \frac{(C_0 - C_e)}{m} \cdot V \quad (2)$$

$q_t$ —sorption capacity in time “ $t$ ”  $\left[\frac{\text{mg}}{\text{g}}\right]$ ,

$q_e$ —equilibrium sorption capacity  $\left[\frac{\text{mg}}{\text{g}}\right]$ ,

$C_0$ —initial mercury concentration  $\left[\frac{\text{mg}}{\text{dm}^3}\right]$ ,

$C_t$ —mercury concentration in time “ $t$ ”  $\left[\frac{\text{mg}}{\text{dm}^3}\right]$ ,

$C_e$ —mercury concentration in equilibrium  $\left[\frac{\text{mg}}{\text{dm}^3}\right]$ ,

$V$ —solution volume  $[\text{dm}^3]$ ,

$m$ —the mass of the bed used in the sorption process [g].

Nonlinear equilibrium models of Langmuir, Freundlich, Dubinin–Radushkevich, Temkin, Hill, Redlich–Peterson, Sips and Toth were determined.

- Langmuir isotherm model

Originally, the isotherm was developed for gas-solid phase adsorption on activated carbon. The model is used to describe chemical adsorption that results in the formation of a monomolecular sorbent layer. The Langmuir isotherm is considered the basic adsorption equation, which is treated as the starting equation for other isotherm models [20];

- Freundlich isotherm model

This is the earliest known relationship that describes non-ideal and reversible adsorption. It applies to multilayer physical adsorption, which occurs on microporous materials with heterogeneous surfaces [21];

- Dubinin–Radushkevich isotherm model

The basic assumption of the Dubinin–Radushkevich isotherm is the occurrence of multilayer adsorption, which involves van der Waals forces and is applicable to the physical adsorption process [22];

- Temkin isotherm model

Temkin’s isotherm is described by a two-parameter equation of monolayer adsorption on a heterogeneous surface. The model assumes that the adsorption energy decreases linearly with increasing sorbent surface coverage due to adsorbent–adsorbate interactions [23];

- Hill isotherm model

Hill’s isotherm analysis is about the explanation of different bindings on homogeneous layers. The model assumes that the adsorption process is cooperative, and that the binding capacity of ligands at a macromolecule site can affect different binding sites on the same molecule [24];

- Redlich–Peterson isotherm model

The model consists of three Langmuir and Freundlich isotherm parameters. The adsorption mechanism is hybrid and deviates from ideal monolayer adsorption. The isotherm equation is valid for both homogeneous and heterogeneous systems analysis [25];

- Sips isotherm model

This isotherm model is used to describe a single-layer adsorption process. It is suitable for analysing adsorption on inhomogeneous surfaces [26];

- Toth isotherm model

The Toth isotherm model is one of the modifications of the Langmuir isotherm model. The main purpose of the modification is to reduce the error between the experimental data and the predicted value. The isotherm can be used when analysing heterogeneous adsorption systems [27].

The equations and parameters for these models are shown in Table 1.

**Table 1.** Equations and parameters of isotherm models.

Model	Nonlinear Equation	Abbreviations
Langmuir	$q = \frac{q_{max} \cdot K_L \cdot C}{1 + K_L \cdot C}$	$q$ —equilibrium sorption capacity [mg/g] $q_{max}$ —maximum sorption capacity [mg/g] $K_L$ —Langmuir constant [dm <sup>3</sup> /mg] $C$ —concentration of adsorbate at equilibrium [mg/dm <sup>3</sup> ]
Freundlich	$q = K_F \cdot C^{1/n}$	$K_F$ —Freundlich constant [dm <sup>3</sup> /g] $n$ —adsorption intensity constant
Dubinin–Radushkevich	$q = q_s \cdot \exp(-K_{DR} \varepsilon^2)$	$K_{DR}$ —Dubinin–Radushkevich constant [mol <sup>2</sup> /kJ <sup>2</sup> ] $q_s$ —isotherm saturation capacity [mg/g] $\varepsilon$ —Polanyi potential [J/mol]
Temkin	$q = \frac{RT}{b_T} \ln(A_T C)$	$A_T, B_T$ —Temkin constants [dm <sup>3</sup> /mg]
Hill	$q = \frac{q_H C^{n_H}}{K_H + C^{n_H}}$	$K_H$ —Hill constant [mg/dm <sup>3</sup> ] $n_H$ —Hill cooperativity coefficient of the binding interaction $q_H$ —Hill sorption capacity [mg/g]

Table 1. Cont.

Model	Nonlinear Equation	Abbreviations
Redlich–Peterson	$q = \frac{K_R \cdot C}{1 + a_R \cdot C^g}$	$K_R$ —Redlich – Peterson constant [ $\text{dm}^3/\text{g}$ ] $a_R$ —constant [ $\text{dm}^3/\text{mg}$ ] $g$ —Redlich Peterson exponent
Sips	$q = \frac{K_S \cdot C^{\beta_s}}{1 + a_S \cdot C^{\beta_s}}$	$K_S$ —Sips constant [ $\text{dm}^3/\text{g}$ ] $a_S$ —Sips constant [ $\text{dm}^3/\text{mg}$ ] $\beta_s$ —Sips exponent
Toth	$q = \frac{K_T \cdot C}{(a_T + C)^{\frac{1}{t}}}$	$K_T$ —Toth constant [ $\text{mg}/\text{g}$ ] $a_T$ —Toth constant [ $\text{dm}^3/\text{mg}$ ] $t$ —Toth heterogeneity factor

### Sorption Kinetics

Based on the obtained results of sorption capacity over time ( $q_t$ ), nonlinear kinetic models of pseudo-first-order, pseudo-second-order, Elovich and intramolecular diffusion were determined.

- Pseudo-first-order model

This model describes adsorption in solid–liquid systems based on the sorption capacity of the sorbent. It assumes that one ion is adsorbed on one independent adsorption site on the sorbent surface. It takes the form of first-order irreversible reaction kinetics, while assuming adsorption as a reversible and equilibrium process [28];

- Pseudo-second-order model

This model describes chemisorption from aqueous solutions. It describes systems where, during the adsorption process, there is a linear relationship between the decrease in the number of available adsorption sites and the decrease in the concentration of adsorbate molecules. It takes the form of second-order irreversible kinetics [29];

- Elovich model

The Elovich model is based on a theory concerning the activation energy of sorption, which it increases as sorption progresses, so that the rate of sorption decreases exponentially [30];

- Intraparticle diffusion model

When analysing the adsorption process, the rate-limiting step can be related to intramolecular diffusion. The model is used to identify the diffusion mechanism that occurs. The process of intramolecular diffusion refers to molecules diffusing from solution to the solid phase and describes adsorption on porous adsorbents [31].

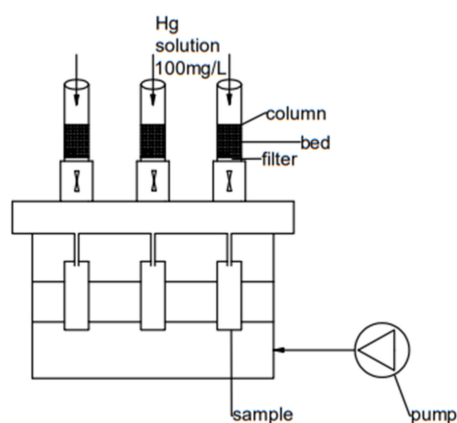
The equations and parameters for these models are shown in Table 2.

Table 2. Equations and parameters of kinetic models.

Model	Equation	Abbreviations
Pseudo-first order	$\frac{dq_t}{dt} = k_I(q - q_t)$	$q_t$ —sorption capacity in time $t$ [ $\text{mg}/\text{g}$ ] $t$ —time of sorption [ $\text{min}$ ] $q$ —equilibrium sorption capacity [ $\text{mg}/\text{g}$ ] $k_I$ —adsorption rate constant of the pseudo – first order model [ $\text{min}^{-1}$ ]
Pseudo-second order	$\frac{dq_t}{dt} = k_{II}(q - q_t)^2$	$k_{II}$ —adsorption rate constant of the pseudo – second order model [ $\text{g}/(\text{mg}\cdot\text{min})$ ]
Elovich	$\frac{dq_t}{dt} = \alpha \cdot \exp(-\beta q_t)$	$\alpha$ —initial adsorption rate [ $\text{mg}/(\text{g}\cdot\text{min})$ ] $\beta$ —adsorption rate constant [ $\text{mg}/\text{g}$ ]
Intraparticle diffusion (Weber–Morris)	$q_t = k_{ID}(t)^{0.5} + I$	$k_{ID}$ —intraparticle diffusion constant [ $\text{min}^{-1}$ ] $I$ —coefficient related to mass transfer through boundary layers [ $\text{mg}/\text{g}$ ] The greater the $I$ constant, the greater the boundary layer effect.

### 2.2.5. Sorption in Flow-Through Column System

Adsorption of mercury from aqueous solution was studied in a flow column system. Measurements were performed in room temperature in a three-column system with a diameter of  $d = 0.6$  cm and a height of  $H = 1.2$  cm (three replications of the test system). A vacuum pump was connected at the bottom to maintain a constant volumetric flow rate in the column system, while an aqueous mercury solution of  $100 \text{ mg/dm}^3$  was continuously fed from the top. Samples of the post-sorption liquid were collected at the bottom of the column at equal time intervals of 2 min and analysed for mercury ion concentration. The total running time of the process was 120 min. A scheme of the column system used for mercury sorption is shown in Figure 1.



**Figure 1.** Scheme of the column system used for mercury sorption on prepared hydrochar.

### Modelling of Continuous Adsorption Process

Designing a fixed bed adsorption column is a complex process. However, a well-developed mathematical model characterised by a high fit to real conditions can help propose a suitable design for a large-scale adsorption column. The performance of an adsorption column is most often represented as a breakthrough curve i.e., a plot of the adsorbate concentration at the outlet of the column versus time. The breakthrough time and the shape of the curve are important parameters explaining the behaviour of an adsorption column. The breakthrough time is the time after which the output concentration of the pollutant reaches the desired limit value. Most often, it is in the range of 1–5% of the feed concentration. Then, as the process runs, the impurity concentration increases from zero/low to a concentration equal to that of the feed. The key factors affecting breakthrough time are column capacity and height, flow rate and feed concentration. These parameters are helpful in determining the total capacity of the column (Maheshwari and Gupta, 2016).

In a flow column system, the following was determined:

Total bed capacity  $q_{tot}$  :

$$q_{tot} = \frac{Q \cdot A}{1000} = \frac{Q}{1000} \int_{t=0}^{t=t_{tot}} C(t) dt \quad (3)$$

where:

$Q$ —volumetric flow rate  $\left[ \frac{\text{cm}^3}{\text{min}} \right]$ ;

$A$ —column cross-sectional area  $[\text{cm}^2]$ ;

$C(t)$ —mercury ion concentration after time  $t$ .

Bed capacity converted to 1 g of sorbent:

$$q_{eq} = \frac{q_{tot}}{m} \quad (4)$$

where:  $m$ —sorbent mass [g]

Total mass of ions adsorbed by the column:

$$m_{tot} = \frac{C_0 \cdot Q \cdot t_{tot}}{1000} \quad (5)$$

where:  $C_0$ —initial mercury solution concentration,  $t_{tot}$  — total sorption time

Total percentage of metal ion removal:

$$Y = \left( \frac{q_{tot}}{m_{tot}} \right) \cdot 100\% \quad (6)$$

It was assumed that bed saturation occurs when the mercury ion concentration reaches 90% of the initial concentration value of  $C_0$ .

The analysis of sorption kinetics in a flow column system was performed on the basis of mathematical models in nonlinear form: Bohart–Adams, Thomas, Yoon–Nelson, Clark, BDST (bed—depth service—time) and Yan. In order to determine the model that best describes sorption on a solid bed in a column, the coefficients of determination— $R^2$  and the root mean square error— $RMSE$  of the analysed models were compared. The model with the  $R^2$  value closest to 1 and the smallest  $RMSE$  error was referred to as the model with the best fit.

- Bohart–Adams model

The Bohart–Adams model is based on the theory of reactions occurring on the surface of the sorbent, and it assumes that the rate of adsorption is directly proportional to the capacity of the sorbent, and that equilibrium is not reached instantaneously. The dynamics of this model is applicable to the analysis of the initial phase of the breakthrough curve, when the adsorbent has the most active sites [32].

- Thomas model

The Thomas model is used to determine the adsorption capacity of the adsorbent and to analyse bed breakthrough curves. An important assumption of this dynamics model is that the process follows pseudo-second-order kinetics and the equilibrium follows the Langmuir isotherm. The Thomas model describes an adsorption process in which all external and internal diffusion resistances are disregarded [33].

- Yoon–Nelson model

This model is characterised by the simplicity of the equation notation compared to the rest of the mathematical models analysed. The main assumption on which Yoon–Nelson is based is that the rate of adsorption decrease for an adsorbate molecule is proportional to the adsorption of the adsorbate and the breakthrough of the adsorbent bed [34].

- Clark model

The basic assumption of the Clark model is based on the fact that the sorption process follows the equilibrium describing the Freundlich isotherm. For this model, the shape of the mass exchange zone is constant, and all adsorbents are eliminated at the end of the column [35].

- BDST model (bed—depth service—time)

The BDST model is used to describe the behaviour of a column with a constant bed height. The equation of the exploitation time of the deposit depth allows for plotting the graph of the dependence of the exploitation time— $t$  as a function of  $C/C_0$ , so that the values of the dynamic parameters of the BDST model can be determined [36].

- Yan model

The Yan model was developed to minimize the errors resulting from the application of the dynamics model described by Thomas. This is particularly important when analysing higher and lower period breakthrough curves [37].

The equations and parameters for these models are shown in Table 3.

**Table 3.** Equations and parameters of dynamic models of the process of sorption of mercury ions on the column.

Model	Nonlinear Equation	Abbreviations
Bohart–Adams	$\frac{C}{C_0} = \frac{\exp(k_{BA} \cdot C_0 \cdot t)}{\exp\left(k_{BA} \cdot q_{max} \cdot \frac{H}{u}\right) - 1 + \exp(k_{BA} \cdot C_0 \cdot t)}$	<p><math>C</math>—effluent adsorbent concentration [mg/dm<sup>3</sup>]  <math>C_0</math>—influent adsorbent concentration [mg/dm<sup>3</sup>]  <math>t</math>—breakthrough time [min]  <math>H</math>—fixed bed depth [cm]  <math>u</math>—linear flow velocity [cm/min]  <math>k_{BA}</math>—Bohart–Adams rate constant model [dm<sup>3</sup>/(min·mg)]  <math>q_{max}</math>—maximum adsorption capacity [mg/g]</p>
Thomas	$\frac{C}{C_0} = \frac{1}{1 + e^{\left(\left(\frac{k_{Th}}{Q}\right) \cdot q_{max} \cdot m - C_0 \cdot k_{Th} \cdot t\right)}}$	<p><math>k_{Th}</math>—Thomas rate constant [dm<sup>3</sup>/(min·mg)]  <math>m</math>—quantity of the adsorbent [g]  <math>Q</math>—flow rate [dm<sup>3</sup>/min]</p>
Yoon–Nelson	$\frac{C}{C_0} = \frac{e^{k_{YN} \cdot (t-\tau)}}{1 + e^{k_{YN} \cdot (t-\tau)}}$	<p><math>k_{YN}</math>—Yoon–Nelson rate constant [1/min]  <math>\tau</math>—the time required for 50% adsorbate breakthrough [min]</p>
Clark	$\frac{C}{C_0} = \left(\frac{1}{1 + A_c \cdot e^{-r \cdot t}}\right)^{\frac{1}{n_F-1}}$	<p><math>A_C</math>—Clark constant [–]  <math>r</math>—Clark constant [1/min]  <math>n_F</math>—Freundlich adsorption intensity constant [–]</p>
BDST	$t = \left(\frac{N_0 \cdot H}{C_0 \cdot u}\right) - \frac{1}{C_0 \cdot k_{BDST}} \cdot \ln\left(\frac{C_0}{C} - 1\right)$	<p><math>k_{BDST}</math>—BDST rate constant [dm<sup>3</sup>/(min·mg)]  <math>N_0</math>—adsorption capacity [mg/dm<sup>3</sup>]</p>
Yan	$\frac{C}{C_0} = 1 - \frac{1}{1 + \left(\frac{C_0 \cdot k \cdot t}{q_{max} \cdot m}\right)^{a_Y}}$	<p><math>a_Y</math>—Yan empirical parameter</p>

### 3. Results and Discussion

#### 3.1. Characterisation of Obtained Hydrochar

No crystalline structures are present in carbon materials such as the obtained hydrochar, as confirmed by the results of XRD analysis shown in Figure 2A. Obtained material exhibits signals at approximately  $2\theta = 23^\circ$  and  $43^\circ$ , which can be indexed as the (002) and (10) graphite-type reflections, respectively [38,39]. Figure 2B shows the results of ATR-FTIR analysis. For spectra shown, characteristic bands can be seen for both the obtained hydrochar and the material after the sorption process. The most intense signals with a maximum at  $1130 \text{ cm}^{-1}$  come from C-O bonds in the alcohol, ester, phenolic and acid groups. Bands around  $2300 \text{ cm}^{-1}$  can be attributed to stretching of nitrile groups. Those groups originate from the naturally derived material from which the hydrochar was obtained. Signals at  $750\text{--}870 \text{ cm}^{-1}$  show the presence of aromatic rings in carbon structures, while bands at  $1560 \text{ cm}^{-1}$  are characteristic of stretching vibrations of C = C bonds present in these rings. In the sample after the sorption process, a broad signal at around  $2600\text{--}3700 \text{ cm}^{-1}$  with a maximum at  $2915 \text{ cm}^{-1}$  is visible, originating from stretching vibrations in O-H and C-H bonds [40–43].

In addition, the point of zero charge (PZC) at room temperature was determined for the obtained material using the pH drift method. The PZC point determined by this method is 7.3, by which it can be concluded that neither positive nor negative charges dominate the surface. This result is similar to the result of 7.6 obtained by Oumabady et al. for hydrochar obtained from paper board mill sludge [44].

BET analysis showed that the resulting hydrochar has a specific surface area of  $145.72 \text{ m}^2/\text{g}$  and an average pore diameter of 1.93 nm. The pore size distribution illustrated in Figure 2D shows that the material is dominated by pores of less than 1 nm in size, so we are dealing with a microporous material. The isothermal adsorption/desorption curve on the hydrochar obtained from apple pomace is shown in Figure 2C and follows a type I

isotherm, while the hysteresis loop corresponds to an H4 type loop. The type I isotherm is used to describe adsorption on microporous materials. It is characterised by monolayer adsorption and shows a fairly rapid increase with pressure and eventually approaches a limit at sufficiently high pressure. The absorption limit depends on the available volume of the micropores [45,46]. The H4 type hysteresis loop is common in micro- and mesoporous adsorbents and in materials having narrow gap pores [43,47,48].

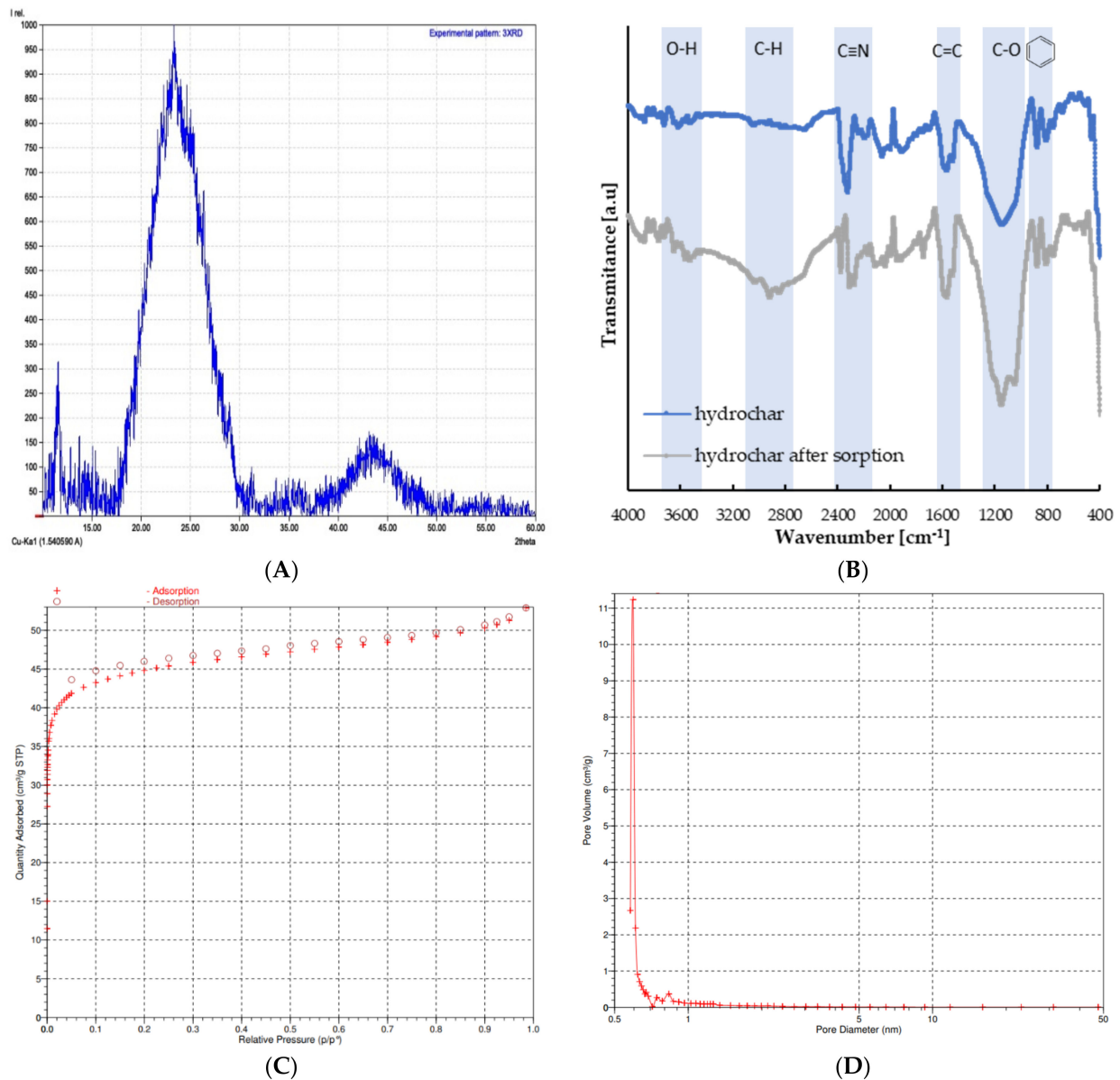


**Figure 2.** (A) XRD diagram of activated hydrochar; (B) ATR-FTIR of hydrochar before and after the mercury sorption process; (C) low temperature nitrogen sorption/desorption isotherm; (D) pore size distribution.

SEM microphotographs before (Figure 3A) and after the sorption process (Figure 3B) show the highly porous structure of the obtained hydrochar, and confirm its stability during the dynamic sorption process. SEM-EDS analysis of the elemental content of the studied surface and near-surface layers of the obtained hydrochar (Figure 3C) showed the presence of trace amounts of elements such as copper, iron, aluminium and silicon. EDS analysis of the material after the sorption process (Figure 3D) showed the presence of mercury and chlorine ions, which are components of the solution used in the sorption process, confirming their sorption on the surface of the material used. The multi-element

mapping performed for the hydrochar after the sorption process (Figure 3E) shows the presence of mercury in the near-surface structures of the material, which also confirms its sorption. The uniform blue coloration seen in the mapping showing the distribution of mercury (Figure 3F) proves that sorption occurs uniformly over the entire surface of the applied material.

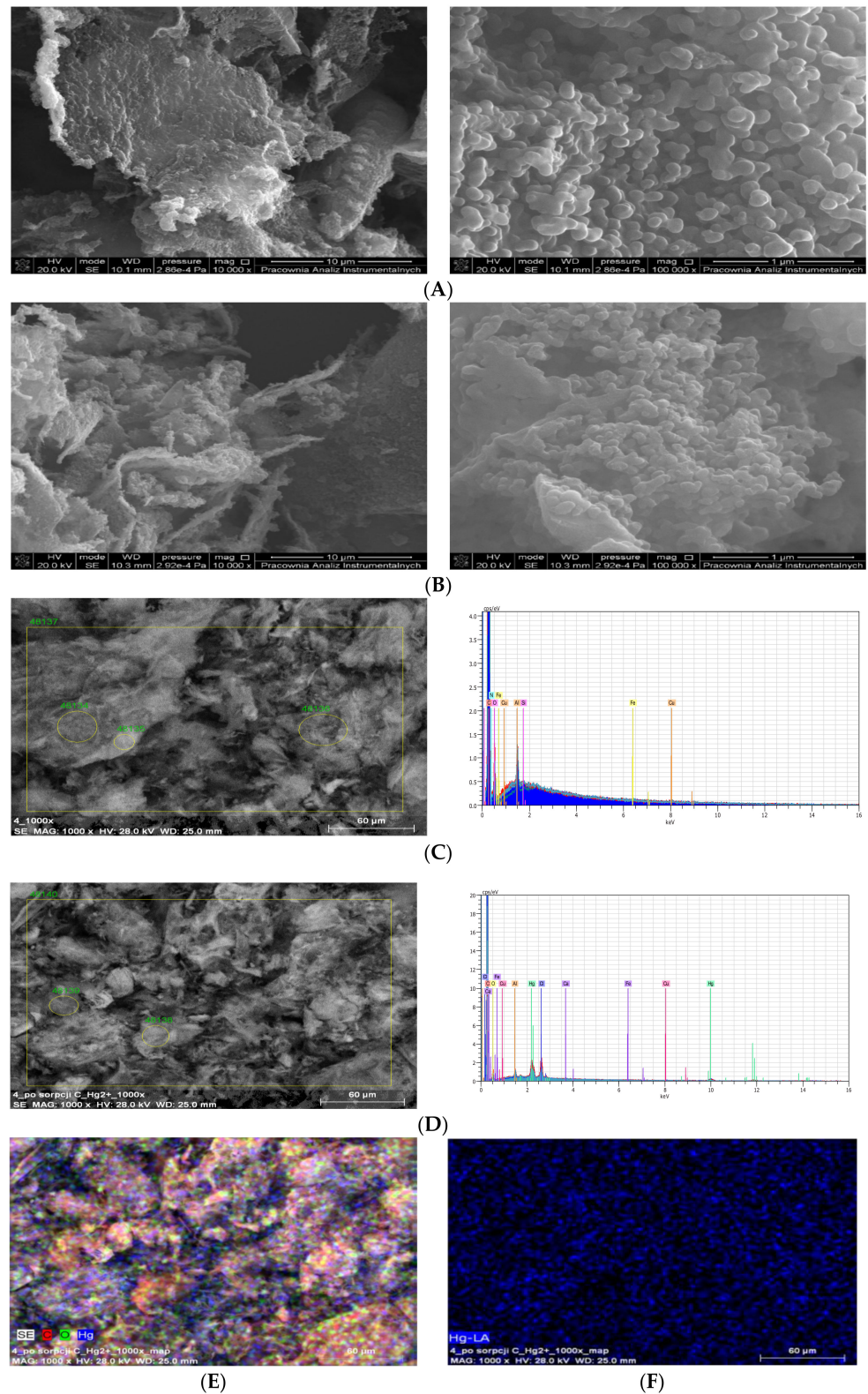


**Figure 3.** SEM microphotographs: (A) obtained hydrochar, (B) hydrochar after mercury sorption,

(C) results of EDS analysis of obtained hydrochar, (D) results of EDS analysis of hydrochar after sorption, (E) mapping of hydrochar after the sorption process, (F) mapping of mercury in hydrochar after sorption process.

### 3.2. Adsorption Isotherm Models

Figure 4 shows the dependence of the sorption capacity on the time of running the sorption process in a batch system. The obtained results confirm that the equilibrium state is reached after 20 min of running the process. Based on the results obtained, nonlinear models of adsorption isotherms were determined. The adsorption isotherm models act as mathematical correlations and play an important role in the model analysis, operational design and practical application of adsorption systems [49]. In order to describe the processes taking place in the solid-liquid system, it is necessary to take into account a number of equilibrium isotherm models. Therefore, in this study it was decided to use two- (Langmuir, Freundlich, Dubinin–Radushkevich, Temkin) and three-parameter (Hill, Redlich–Peterson, Sips, Toth) models describing both chemical processes and those taking into account physicochemical interactions. The models are shown in Figure 5, while the determined parameters are listed in Table 4.

After analysing the values of the root mean squared error— $RMSE$  and the coefficients of determination— $R^2$  located in Table 4, the best fit of the sorption isotherm model was determined. The highest values of  $R^2 = 0.9918$ , while the smallest values of  $RMSE = 1.535$  are characterised by the Freundlich, Sips and Toth isotherm models. The Freundlich isotherm describes the process of multilayer sorption on heterogenic surfaces. The parameter  $n$  determines the inhomogeneity of the surface and the exponential distribution of active sites and their energies. The resulting value of  $n > 1$  ( $n = 2.791$ ) indicates a more convex isotherm, which is favourable for typical adsorption processes. Moreover, the model assumes that the process involves multilayer physical adsorption, which is reversible and occurs on microporous materials [50]. The Sips isotherm is a combination of the Langmuir and Freundlich isotherms. This model is suitable for predicting adsorption on heterogeneous surfaces, bypassing the limitation of increasing adsorbate concentration that is usually associated with the Freundlich model [51]. Toth's model describes heterogeneous adsorption systems well, for both low and high adsorbate concentrations. The parameter  $T$  characterizes the heterogeneity of the adsorption system, and if it deviates from unity (1), as in the case of this work ( $T = 1.558$ ) then this indicates the heterogeneity of the system [52].

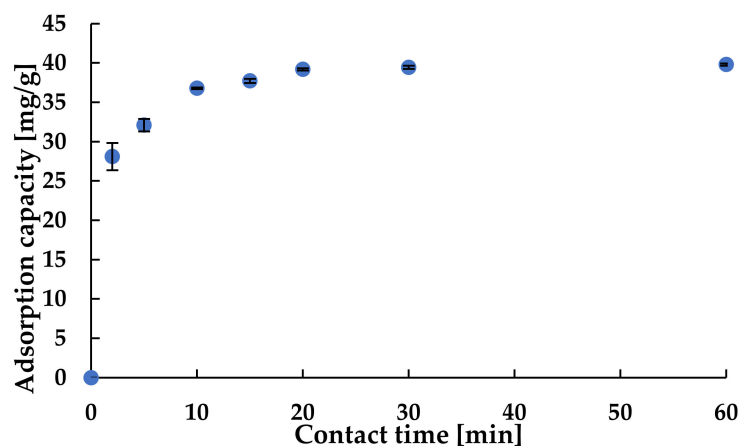


Figure 4. Plot of sorption capacity versus time for a 100 mg/dm<sup>3</sup> mercury solution.

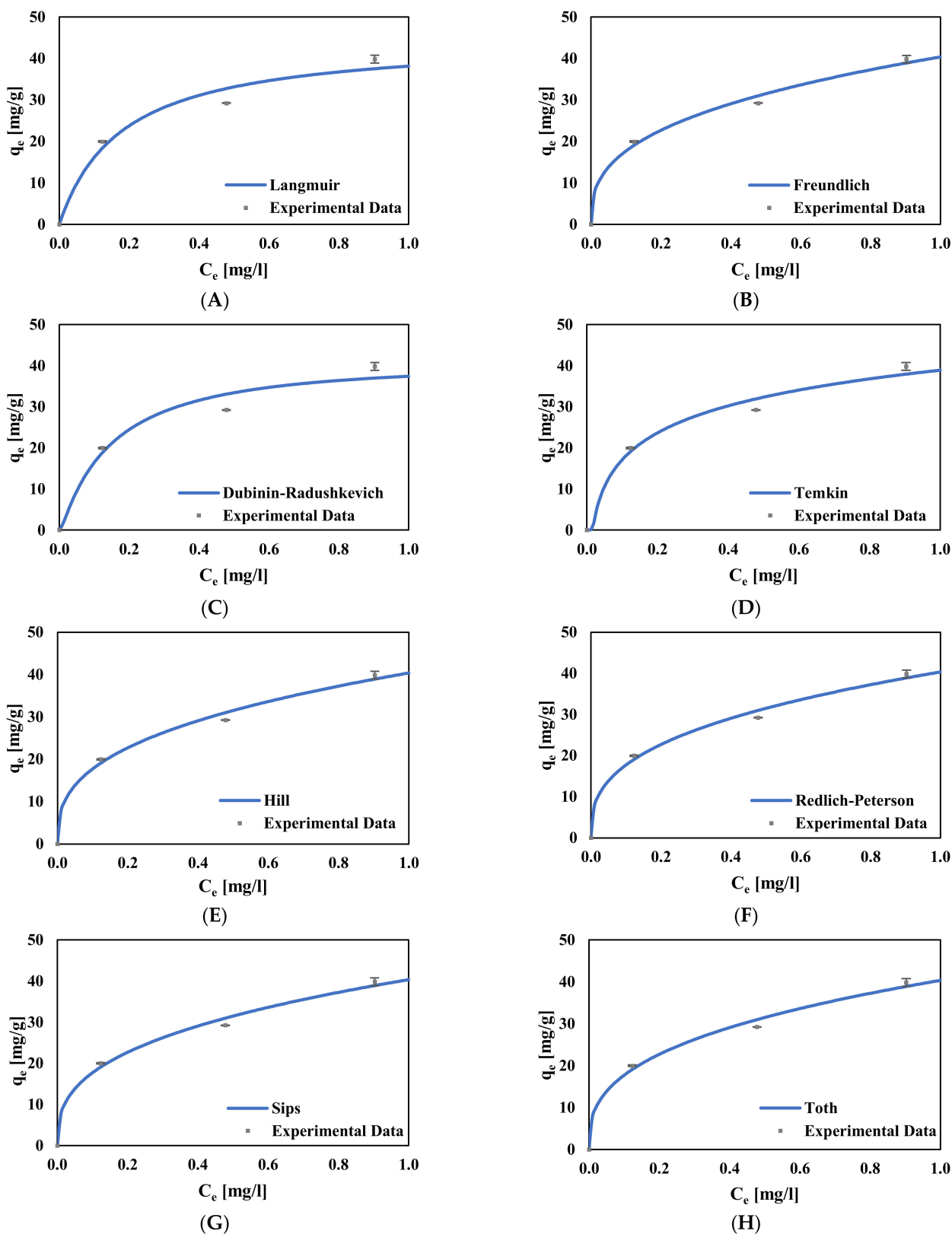


Figure 5. Nonlinear isotherm models: (A) Langmuir, (B) Freundlich, (C) Dubinin–Radushkevich, (D) Temkin, (E) Hill, (F) Redlich-Peterson, (G) Sips, (H) Toth.

**Table 4.** Parameters of the determined nonlinear equilibrium models.

Model	Parameters	Result
Langmuir	$q_{max}$ [mg/g]	44.93
	$K_L$ [dm <sup>3</sup> /mg]	5.613
	$R^2$	0.9650
	RMSE	3.165
Freundlich	$K_F$ [dm <sup>3</sup> /g]	40.32
	$n$ [–]	2.791
	$R^2$	0.9918
	RMSE	1.535
Dubinin–Radushkevich	$K_{DR}$ [mol <sup>2</sup> /kJ <sup>2</sup> ]	0.02627
	$q_s$ [mg/g]	40.31
	$R^2$	0.8783
	RMSE	4.901
Temkin	$A_T$ [dm <sup>3</sup> /mg]	60.52
	$b_T$ [dm <sup>3</sup> /mg]	256.8
	$R^2$	0.9415
	RMSE	3.398
Hill	$K_H$ [mg/dm <sup>3</sup> ]	1518
	$n_H$ [–]	0.3585
	$q_{SH}$ [mg/g]	$6.13 \times 10^4$
	$R^2$	0.9835
Redlich-Peterson	RMSE	2.171
	$K_R$ [dm <sup>3</sup> /g]	$3.31 \times 10^6$
	$a_R$ [dm <sup>3</sup> /mg]	82090
	$G$	0.6417
Sips	$R^2$	0.9835
	RMSE	2.171
	$K_S$ [dm <sup>3</sup> /g]	40.32
	$a_s$ [dm <sup>3</sup> /mg]	$6.15 \times 10^{-13}$
Toth	$\beta_s$ [–]	0.3583
	$R^2$	0.9918
	RMSE	1.535
	$K_T$ [mg/g]	40.32
Toth	$a_T$ [dm <sup>3</sup> /mg]	$1.13 \times 10^{-11}$
	$t$ [–]	1.558
	$R^2$	0.9918
	RMSE	1.535

The high values of the coefficients  $R^2 = 0.9835$ , and at the same time the low error values  $RMSE = 2.171$  of the Hill and Redlich-Peterson models demonstrate also a good fit of these theoretical models to experimental data. Hill's model describes adsorption as a cooperative phenomenon, where adsorbed molecules on the surface of an adsorbent interact with other active sites in the same adsorbent. The Redlich-Peterson model combines assumptions from Langmuir and Freundlich isotherms and assumes mixed adsorption mechanisms. The Langmuir model also shows a good fit achieving a determination coefficient of  $R^2 = 0.965$ . It describes systems where monolayer adsorption occurs on a homogeneous surface with no interaction between adsorbed ions. In addition, the theoretical value of  $q_{max} = 44.93$  mg/g determined from this model is close to the experimentally obtained values of 39.82 mg/g.

Mercury forms monovalent and divalent compounds with fluorine, chlorine, bromine, iodine, and sulphur, among others [53]. In addition, mercury, like other metals, especially heavy metals, in ionic form has a high affinity for complex or chelate groups (such as carboxyl groups, hydroxyl groups, etc. located on the surface of hydrocarbons) present in systems, binding to it in the form of complexes [54]. This property is widely used in

sorbent modifications that are able to immobilise metal ions and enable the removal of these species from aqueous media. When chemical bonds are formed, covalent coordination bonds are formed between metal cations and groups immobilised on the surface of the adsorbent, acting as Lewis bases. Lewis bases (e.g., N-, O-, S-, P-containing groups, etc.) have nonbonding electrons that can be shared with, for example, metal cations by means of a covalent bond, thus guaranteeing stable immobilisation of metal species on the adsorbent. In the case of physical processes, the simple formation of multi-layered cations is unlikely due to positive charge repulsion. Alternate formation of cation and anion layers seems more reasonable. As the surface of a material becomes saturated with metal ions, it becomes intensely positively charged and an electrostatic imbalance is created in the aqueous environment. Consequently, the positively charged particles of the material begin to adsorb superior anions from solution through physisorption and become negatively charged.

In the presented study, the high degree of fit between several theoretical models and the obtained experimental data demonstrates the presence of combined mechanisms of mercury adsorption on the obtained hydrochar and proves the high complexity of the process. The possibility of multilayers in the sorption of heavy metal ions, e.g., Cu(II) and Cd(II), was confirmed by Jorgetto et al. The authors noted that the transition points between monolayer and multilayer occur at different initial concentrations of metal ions and depend on additional factors, including the ratio of deposit to ion, ion concentration in solution, and type of ion. This can be explained by fundamentals in the ionic radii of metals. As the ionic radius increases, the ions are affected by greater steric hindrance and the surface of the material will reach saturation of the monolayer at a lower concentration compared to ions of smaller size. These effects will be balanced by the slower arrival of ions at the active sites resulting from the larger volume and mass of the molecules [55]. Imla Syafiqah and Yussof compared the degree of fit of experimental data to Langmuir and Freundlich adsorption isotherm models in the removal of mercury ions from aqueous solution using modified palm oil fuel ash. The authors confirmed that the Langmuir model based on adsorbate monolayer is only beneficial for a homogeneous surface. The Freundlich model suggests neither homogeneous energy sites nor limited levels of adsorption. This means that the Freundlich model can describe the experimental data of adsorption isotherms regardless of whether adsorption occurs on homogeneous or heterogeneous surfaces and is not controlled by monolayer formation [56]. In addition, the results of Mapombere et al. show that mercury adsorption on *Pterocarpus Anglensis* is best described by the Freundlich isotherm [57], and the  $n$  value (2.93) was close to that obtained in the study presented in this paper. Mohammadnia et al. performed mercury sorption on thiolated Fe<sub>3</sub>O<sub>4</sub>/graphene oxide nanoparticles. The sorption process was best described by the Langmuir model ( $R^2 = 0.995$ ). The maximum theoretical sorption capacity determined from the Langmuir model was 129.7 mg/g, which is higher than the values obtained experimentally (95.3 mg/g). At the same time, the Freundlich model also had a high degree of fit ( $R^2 = 0.982$ ), which confirms that the process of mercury sorption on carbon materials is a complex process and occurs on the basis of mixed mechanisms [58].

### 3.3. Adsorption Kinetic Models

Figure 6 shows the nonlinear kinetic pseudo-first-order, pseudo-second-order, Elovich and intraparticle diffusion models, while the calculated parameters of the kinetic models are summarised in Table 5. As in the case of the equilibrium analysis, the model with the  $R^2$  value closest to 1 and the smallest *RMSE* error was referred to as the best-fit model. In addition, in order to better understand the mechanics of the process taking place, a linear interpretation of the intramolecular diffusion model was plotted, as shown in Figure 6D.

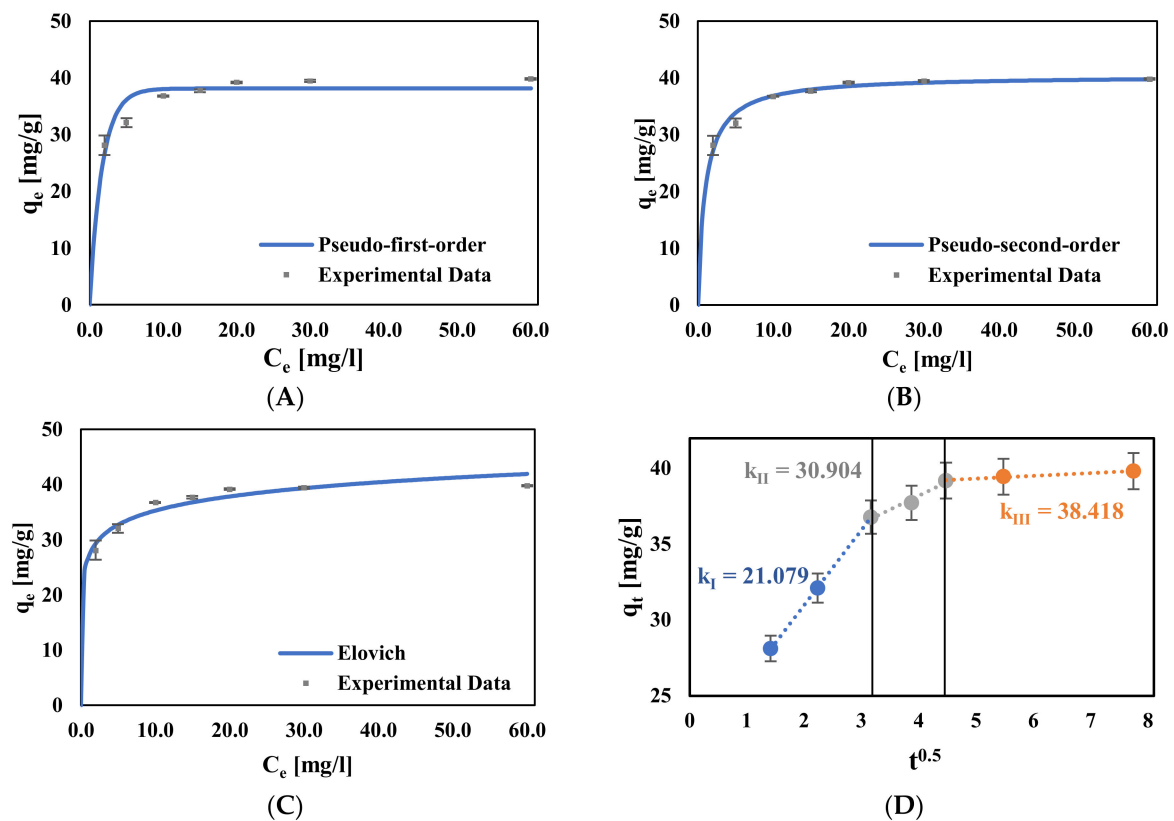


**Figure 6.** Kinetic nonlinear models: (A) pseudo-first-order; (B) pseudo-second-order; (C) Elovich; (D) linear model of intramolecular diffusion.

**Table 5.** Parameters of the determined nonlinear kinetic models.

Model	Parameters	Results
Pseudo-first-order	$q_{max}$ [mg/g]	38.11
	$k_I$ [1/min]	0.5882
	$R^2$	0.9789
	RMSE	2.105
Pseudo-second-order	$q_{max}$ [mg/g]	40.40
	$k_{II}$ [g/(mg·min)]	0.0255
	$R^2$	0.9965
	RMSE	0.8600
Elovich	$\alpha$ [mg/(g·min)]	5040
	$\beta$ [g/mg]	0.2697
	$R^2$	0.9911
	RMSE	1.368
Intraparticle diffusion	$k_{ID}$ [1/min]	0.1003
	$I$ [mg/g]	27.88
	$R^2$	0.9881
	RMSE	1.583
Experimental data	$q_{max}$ [mg/g]	39.82

Based on the analysis of the kinetic parameters in Table 5, the best fit of the kinetic model occurs for the pseudo-second-order model. This model has the highest value of the coefficient of determination ( $R^2 = 0.9965$ ) and the smallest value of the root mean square error ( $RMSE = 0.8600$ ). In addition, the theoretically determined sorption capacity of 40.40 mg/g is close to the experimentally obtained result of 39.82 mg/g. According to the assumptions of this model, the process is chemical in nature. This is due to the

presence of functional groups on the surface of the material derived from the organic matter from which the analysed hydrochar was obtained. A high degree of fit is also shown by the Elovich kinetic models ( $R^2 = 0.9911$ ) and the pseudo-first-order model ( $R^2 = 0.9789$ ); however, the *RMSE* errors for these models are higher than for the pseudo-second-order model. Nevertheless, this indicates that the process follows mixed mechanisms, among which there is not one definitely dominant one.

The kinetics of adsorption can be limited by the different steps of adsorption, so the linear kinetic model of intramolecular diffusion was used to identify this issue in more depth. The linear form of the intramolecular diffusion model revealed that the adsorption process occurs in three steps. The first step is related to diffusion at the interface, where diffusion of the adsorbate to the outer layer of the adsorbent takes place. The second step involves diffusion into the pores of the adsorbent, while the final step is the deposition of the adsorbate inside the structure of the material [59]. None of the determined straight lines aim to intersect the beginning of the coordinate system, which means that intramolecular diffusion is not the only limiting step in the adsorption process and diffusion in the boundary layer can also affect the adsorption process [60]. The slope of the first curve is much higher than that of the second curve, indicating a higher rate of the boundary diffusion step compared to intramolecular diffusion. The intramolecular diffusion step needs considerably more time due to the very slow diffusion of adsorbates from the surface layer into the micropores, which are less accessible adsorption sites. The almost zero slope of the curve in the third stage indicates that the adsorption equilibrium state has been reached [61,62].

Additionally the comparison to other hydrochars obtained by scientists have been conducted, which is concluded in Table 6.

**Table 6.** Comparison to other hydrochars available in the literature.

Source Material	Hydrothermal Process Conditions	Maximum Adsorption Capacity	Authors
Apple pomace	High-pressure hydrothermal reactor, 230 °C, 5 h, Solid:liquid ratio 1:8.75	39.8 mg/g for Hg <sup>2+</sup> (batch)	This paper
Rice straw	Microwave assisted process, 160–200 °C, 40–70 min, solid:liquid ratio 1:10	112.8 mg/g for Zn <sup>2+</sup> 144.9 mg/g for Cu <sup>2+</sup> 222.1 mg/g for Congo Red 174.0 mg/g for berberine hydrochloride 48.7 mg/g for 2-naphtol	[63]
Palm kernel shells	High-pressure hydrothermal reactor, 200 °C, 4 h, solid:liquid ratio 1:5	13.2 mg/g for diclofenac	[64]
Bamboo + PVA	Electric furnace, 200 °C, 24 h, solid:liquid ratio 1:5	259.0 mg/g for Methylene blue	[65]
Rice straw	Tubular sealed reactor, 200 °C, 3 h, solid:liquid ratio 1:3	6.7 mg/g for Pb <sup>2+</sup> 2.7 mg/g for Cu <sup>2+</sup>	[66]
Avocado seed	Hydriion Scientific reactor, 250 °C, 12 h, solid:liquid ratio 1.5:1	20.5 mg/g for Ni <sup>2+</sup> 49.7 mg/g for Pb <sup>2+</sup> 12.7 mg/g for Cu <sup>2+</sup>	[67]
Corn cob straw	Hydrothermal reactor, 200 °C, 30 min, solid:liquid ratio 1:6	207.6 mg/g to Zn <sup>2+</sup> 56.1 mg/g to Cu <sup>2+</sup>	[68]

### 3.4. Fixed-Bed Column Modelling

In order to test the applicability of the obtained material also in flow processes, a continuous sorption process was carried out on a solid bed column. Figure 7 shows

the plot of  $C/C_0$  versus the time of conducting sorption on the column illustrating the sorption dynamics models on the obtained hydrochar. The parameters determined from the equations of the sorption dynamics models are summarised in Table 7.

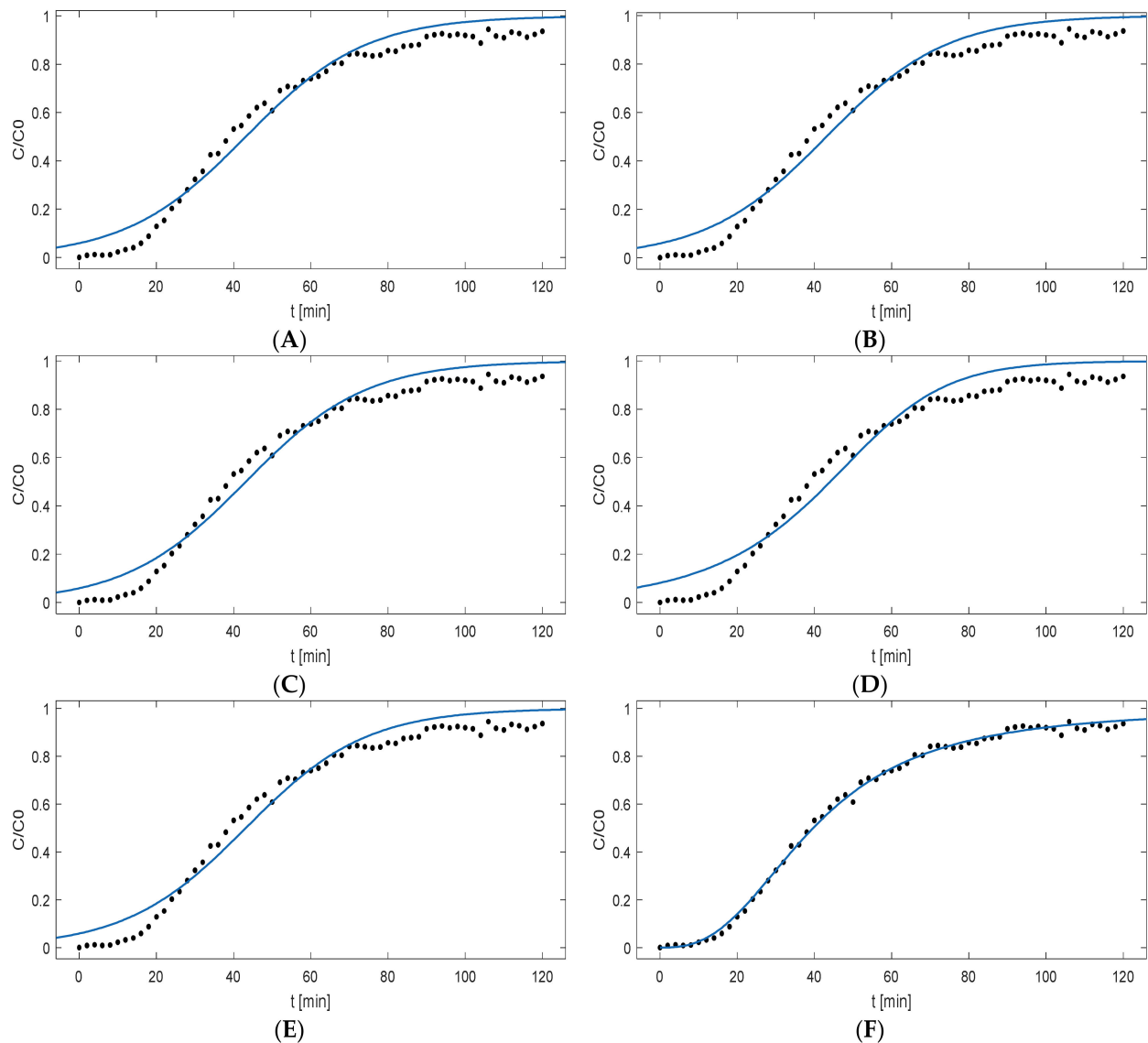


**Figure 7.** Graphical representation of models describing sorption of mercury on a hydrochar bed column system: (A) Bohart–Adams; (B) Thomas; (C) Yoon–Nelson; (D) Clark; (E) BDST; (F) Yan.

The coefficients of determination shown in Table 7 indicate that the Yan model ( $R^2 = 0.9976$ ) best describes the breakthrough curves of the mercury sorption process on the hydrochar-filled column. In addition, this model has the smallest *RMSE* error (0.0165), so that the predictions of the Yan model are closer to the experimental breakthrough curves compared to the other models. This is particularly evident in the lower and upper ranges of the breakthrough curves, where the predictions of the other analysed models deviated from the experimental values, while the curve determined from the Yan model predicts the realistically obtained values very well. In the case of maximum adsorption capacity, the value determined from the Thomas model ( $q_{max} = 111.5$  mg/g) was closer to the experimentally obtained results ( $q_{max} = 116.9$  mg/g), compared to that obtained from the Yan model ( $q_{max} = 102.8$  mg/g). This means that the Thomas model can be used to determine the maximum capacity of the bed with high accuracy, while the Yan model better represents the

course of the sorption process carried out. The results obtained in this work are consistent with the data available in the literature.

**Table 7.** Parameters determined for mathematical models describing mercury sorption on a hydrochar bed column.

Model	Parameter	Results
Bohart-Adams	$k_{BA}$ [ $\text{dm}^3 / (\text{min} \cdot \text{mg})$ ]	0.6635
	$q_{max}$ [ $\text{mg}/\text{g}$ ]	31.25
	$R^2$	0.9710
	RMSE	0.0579
Thomas	$k_{TH}$ [ $\text{dm}^3 / (\text{min} \cdot \text{mg})$ ]	0.6660
	$q_{max}$ [ $\text{mg}/\text{g}$ ]	111.5
	$R^2$	0.9710
	RMSE	0.0579
Yoon-Nelson	$k_{YN}$ [ $1/\text{min}$ ]	0.0643
	$\tau$ [ $\text{min}$ ]	43.16
	$R^2$	0.9710
	RMSE	0.0579
Clark	$A_c$ [–]	89.08
	$r$ [ $1/\text{min}$ ]	0.0814
	$R^2$	0.9569
	RMSE	0.0705
BDST	$k_{BDST}$ [ $\text{dm}^3 / (\text{min} \cdot \text{mg})$ ]	0.6636
	$N_0$ [ $\text{mg}/\text{L}$ ]	111.9
	$R^2$	0.9710
	RMSE	0.0579
Yan	$a_Y$ [–]	2.647
	$q_{max}$	102.8
	$R^2$	0.9976
	RMSE	0.0165

Ghasemi et al. performed mercury adsorption on magnetised single-walled carbon nanotubes (SWCNTs) functionalised with polydopamine. Studies of isotherms and adsorption kinetics showed that the mercury sorption process follows the Freundlich adsorption isotherm and pseudo-second-order kinetic model. The Thomas model proved to predict more accurate results for the maximum adsorption of mercury ions. Based on the high coefficients of determination of  $R^2 = 0.946\text{--}0.978$  for the Thomas model and  $R^2 = 0.955\text{--}0.990$  for the Yan model, respectively, both models were found to have a good fit to mercury sorption data on a fixed bed reactor [69]. Hadavifar et al. performed mercury sorption on multi-walled carbon nanotubes functionalised with amine and thiol groups. The obtained nonlinear regression correlation coefficients from the Yan model ( $R^2 = 0.957\text{--}0.999$ ) compared to those obtained for the Thomas model ( $R^2 = 0.978\text{--}0.996$ ) are slightly higher, except in two cases. As in the case of this work, the obtained data were slightly better fitted by the Yan model than by the Thomas model; however, the differences between the experimental adsorption capacity and the values predicted by the Thomas model are smaller than in the case of the Yan model [70].

#### 4. Conclusions

The main objective of this study was to identify the possibility of using hydrochar obtained from waste of natural origin to eliminate mercury ions from aqueous systems in a batch and flow-through column system. The obtained material was characterised by ATR-FTIR, SEM-EDS, BET and XRD analyses, which confirmed the obtaining of a highly porous carbon material with a specific surface area of  $145.72 \text{ m}^2/\text{g}$  and an average pore diameter of  $1.93 \text{ nm}$ . Equilibrium and kinetic sorption parameters were determined for

the obtained hydrochar using the batch sorption method, and a flow sorption process was carried out on a solid bed column system. The sorption process of mercury on the obtained material is best described using the Freundlich isotherm and a pseudo-second-order kinetic model. This allows us to conclude that the process is mainly chemical in nature; however, the high coefficients of determination also obtained for several other isotherms (Sips, Toth, Hill, Redlich–Peterson and Langmuir) and kinetic models (Elovich and pseudo-first-order) suggest that the sorption process occurs according to combined mechanisms and shows a high level of complexity. Dynamics determined from column tests showed that the Yan model has the best fit across the study area, although it is the Thomas model that better predicts the maximum capacity of the bed. It can be concluded that the hydrochar obtained from apple pomace by hydrothermal carbonisation and then activated by physical method fulfils its role as a sorbent of  $\text{Hg}^{2+}$  ions from aqueous solutions, so that it can be used for their reduction or elimination in both batch and flow-through processes on a solid bed column.

**Author Contributions:** Conceptualization, M.B.; methodology, M.B., K.S.; software, G.H., O.D., K.S.; validation, G.H., K.S.; formal analysis, M.B., G.H., O.D., K.S., J.P.-P.; investigation, G.H., K.S.; data curation, G.H., K.S.; writing—original draft preparation, K.S., G.H.; writing—review and editing, K.S., O.D., J.P.-P., M.B.; visualization, G.H., K.S., O.D.; supervision, M.B. All authors have read and agreed to the published version of the manuscript.

**Funding:** This research received no external funding. This research did not receive any specific grant from funding agencies in the public, commercial, or not-for-profit sector.

**Conflicts of Interest:** The authors report no declarations of interest.

## References

1. Attard, T.; Attard, E. Heavy Metals in Cosmetics. In *Heavy Metals—New Insights*; IntechOpen: Vienna, Austria, 2022; pp. 1–21. [[CrossRef](#)]
2. Hale, R.C.; King, A.E.; Ramirez, J.M.; La Guardia, M.; Nidel, C. Durable Plastic Goods: A Source of Microplastics and Chemical Additives in the Built and Natural Environments. *Environ. Sci. Technol. Lett.* **2022**, *9*, 798–807. [[CrossRef](#)]
3. Pratiwi, R.; Auliya As, N.N.; Yusar, R.F.; Shofwan, A.A. Analysis of Prohibited and Restricted Ingredients in Cosmetics. *Cosmetics* **2022**, *9*, 87. [[CrossRef](#)]
4. Hylander, L.D.; Meili, M. 500 Years of Mercury Production: Global Annual Inventory by Region until 2000 and Associated Emissions. *Sci. Total Environ.* **2003**, *304*, 13–27. [[CrossRef](#)]
5. Harada, M. Minamata Disease: Methylmercury Poisoning in Japan Caused by Environmental Pollution. *Crit. Rev. Toxicol.* **1995**, *25*, 1–24. [[CrossRef](#)]
6. World Health Organization. *Preventing Disease through Healthy Environments: Exposure to Mercury: A Major Public Health Concern*, 2nd ed.; World Health Organization: Geneva, Switzerland, 2021.
7. World Health Organization. *Preventing Disease through Healthy Environments: Exposure to Mercury: A Major Public Health Concern*; World Health Organization: Geneva, Switzerland, 2007.
8. Puścion-Jakubik, A.; Mielech, A.; Abramiuk, D.; Iwaniuk, M.; Grabia, M.; Bielecka, J.; Markiewicz-Żukowska, R.; Socha, K. Mercury Content in Dietary Supplements From Poland Containing Ingredients of Plant Origin: A Safety Assessment. *Front. Pharmacol.* **2021**, *12*, 2832. [[CrossRef](#)]
9. Raj, D.; Maiti, S.K. Sources, Toxicity, and Remediation of Mercury: An Essence Review. *Environ. Monit. Assess.* **2019**, *191*, 566. [[CrossRef](#)]
10. Yu, J.G.; Yue, B.Y.; Wu, X.W.; Liu, Q.; Jiao, F.P.; Jiang, X.Y.; Chen, X.Q. Removal of Mercury by Adsorption: A Review. *Environ. Sci. Pollut. Res.* **2016**, *23*, 5056–5076. [[CrossRef](#)]
11. Xia, S.; Huang, Y.; Tang, J.; Wang, L. Preparation of Various Thiol-Functionalized Carbon-Based Materials for Enhanced Removal of Mercury from Aqueous Solution. *Environ. Sci. Pollut. Res.* **2019**, *26*, 8709–8720. [[CrossRef](#)]
12. Fabre, E.; Lopes, C.B.; Vale, C.; Pereira, E.; Silva, C.M. Valuation of Banana Peels as an Effective Biosorbent for Mercury Removal under Low Environmental Concentrations. *Sci. Total Environ.* **2020**, *709*, 135883. [[CrossRef](#)]
13. Foroutan, R.; Mohammadi, R.; Farjadfar, S.; Esmaili, H.; Ramavandi, B.; Sorial, G.A. Eggshell Nano-Particle Potential for Methyl Violet and Mercury Ion Removal: Surface Study and Field Application. *Adv. Powder Technol.* **2019**, *30*, 2188–2199. [[CrossRef](#)]
14. Hashemi, S.A.; Mousavi, S.M.; Ramakrishna, S. Effective Removal of Mercury, Arsenic and Lead from Aqueous Media Using Polyaniline-Fe<sub>3</sub>O<sub>4</sub>-Silver Diethyldithiocarbamate Nanostructures. *J. Clean. Prod.* **2019**, *239*, 118023. [[CrossRef](#)]
15. Fausey, C.L.; Zucker, I.; Lee, D.E.; Shaulsky, E.; Zimmerman, J.B.; Elimelech, M. Tunable Molybdenum Disulfide-Enabled Fiber Mats for High-Efficiency Removal of Mercury from Water. *ACS Appl. Mater. Interfaces* **2020**, *12*, 18446–18456. [[CrossRef](#)]

16. Yu, J.; Zhu, Z.; Zhang, H.; Di, G.; Qiu, Y.; Yin, D.; Wang, S. Hydrochars from Pinewood for Adsorption and Nonradical Catalysis of Bisphenols. *J. Hazard. Mater.* **2020**, *385*, 121548. [[CrossRef](#)]
17. Zulkornain, M.F.; Shamsuddin, A.H.; Normanbhay, S.; Md Saad, J.; Ahmad Zamri, M.F.M. Optimization of Rice Husk Hydrochar via Microwave-Assisted Hydrothermal Carbonization: Fuel Properties and Combustion Kinetics. *Bioresour. Technol. Rep.* **2022**, *17*, 100888. [[CrossRef](#)]
18. Gascó, G.; Paz-Ferreiro, J.; Álvarez, M.L.; Saa, A.; Méndez, A. Biochars and Hydrochars Prepared by Pyrolysis and Hydrothermal Carbonisation of Pig Manure. *Waste Manag.* **2018**, *79*, 395–403. [[CrossRef](#)]
19. Fu, M.M.; Mo, C.H.; Li, H.; Zhang, Y.N.; Huang, W.X.; Wong, M.H. Comparison of Physicochemical Properties of Biochars and Hydrochars Produced from Food Wastes. *J. Clean. Prod.* **2019**, *236*, 117637. [[CrossRef](#)]
20. Langmuir, I. The Adsorption of Gases on Plane Surfaces of Glass, Mica and Platinum. *J. Am. Chem. Soc.* **1918**, *40*, 1361–1403. [[CrossRef](#)]
21. Holmes, H.N. Colloid and Capillary Chemistry. By Herbert Freundlich. Translated from the Third German Edition by H. Stafford Hatfield. New York, E. P. Dutton and Company, 1926. 886 Pages, 156 Figures. *Science* **1927**, *65*, 40–41. [[CrossRef](#)]
22. Dubinin, M.M. The Potential Theory of Adsorption of Gases and Vapors for Adsorbents with Energetically Nonuniform Surfaces. *Chem. Rev.* **1960**, *60*, 235–241. [[CrossRef](#)]
23. Temkin, M.J.; Pyzhev, V. Kinetics of Ammonia Synthesis on Promoted Iron Catalyst. *Acta Phys. Chim.* **1940**, *12*, 327–356.
24. Hill, T.L. Statistical Mechanics of Multimolecular Adsorption. I. *J. Chem. Phys.* **1946**, *14*, 263–267. [[CrossRef](#)]
25. Redlich, O.; Peterson, D.L. A Useful Adsorption Isotherm. *J. Phys. Chem.* **1959**, *63*, 1024. [[CrossRef](#)]
26. Sips, R. On the Structure of a Catalyst Surface. *J. Chem. Phys.* **1948**, *16*, 490–495. [[CrossRef](#)]
27. Jaroniec, M.; Tóth, J. Adsorption of Gas Mixtures on Heterogeneous Solid Surfaces: I. Extension of Tóth Isotherm on Adsorption from Gas Mixtures. *Colloid Polym. Sci. Kolloid Zeitschrift Zeitschrift Polym.* **1976**, *254*, 643–649. [[CrossRef](#)]
28. Lagergren, S.K. About the Theory of So-Called Adsorption of Soluble Substances. *Sven. Vetenskapsakad. Handlingar* **1898**, *24*, 1–39.
29. Ho, Y.S.; McKay, G. A Comparison of Chemisorption Kinetic Models Applied to Pollutant Removal on Various Sorbents. *Process Saf. Environ. Prot.* **1998**, *76*, 332–340. [[CrossRef](#)]
30. Gundry, P.M.; Tompkins, F.C. Chemisorption of Gases on Metals. *Q. Rev. Chem. Soc.* **1960**, *14*, 257–291. [[CrossRef](#)]
31. Weber, T.W.; Chakravorty, R.K. Pore and Solid Diffusion Models for Fixed-bed Adsorbents. *AIChE J.* **1974**, *20*, 228–238. [[CrossRef](#)]
32. Bohart, G.S.; Adams, E.Q. Some Aspects of the Behavior of Charcoal with Respect to Chlorine. *J. Am. Chem. Soc.* **1920**, *42*, 523–544. [[CrossRef](#)]
33. Thomas, H.C. Chromatography: A Problem in Kinetics. *Ann. N. Y. Acad. Sci.* **1948**, *49*, 161–182. [[CrossRef](#)] [[PubMed](#)]
34. Yoon, Y.H.; Nelson, J.H. Application of Gas Adsorption Kinetics I. A Theoretical Model for Respirator Cartridge Service Life. *Am. Ind. Hyg. Assoc. J.* **1984**, *45*, 509–516. [[CrossRef](#)] [[PubMed](#)]
35. Clark, R.M. Evaluating the Cost and Performance of Field-Scale Granular Activated Carbon Systems. *Environ. Sci. Technol.* **1987**, *21*, 573–580. [[CrossRef](#)] [[PubMed](#)]
36. Hutchins, R.A. New Simplified Design of Activated Carbon System. *Am. J. Chem. Eng.* **1973**, 133–138.
37. Yan, G.; Viraraghavan, T.; Chen, M. A New Model for Heavy Metal Removal in a Biosorption Column. *Adsorpt. Sci. Technol.* **2001**, *19*, 25–43. [[CrossRef](#)]
38. Chen, J.; Zhang, L.; Yang, G.; Wang, Q.; Li, R.; Lucia, L.A. Preparation and Characterization of Activated Carbon from Hydrochar by Phosphoric Acid Activation and Its Adsorption Performance in Prehydrolysis Liquor. *BioResources* **2017**, *12*, 5928–5941. [[CrossRef](#)]
39. Jurkiewicz, K.; Pawlyta, M.; Burian, A. Structure of Carbon Materials Explored by Local Transmission Electron Microscopy and Global Powder Diffraction Probes. *C* **2018**, *4*, 68. [[CrossRef](#)]
40. Ameen, M.; Zamri, N.M.; May, S.T.; Azizan, M.T.; Aqsha, A.; Sabzoi, N.; Sher, F. Effect of Acid Catalysts on Hydrothermal Carbonization of Malaysian Oil Palm Residues (Leaves, Fronds, and Shells) for Hydrochar Production. *Biomass Convers. Biorefinery* **2022**, *12*, 103–114. [[CrossRef](#)]
41. Cui, X.; Gai, D.; Zhu, B.; Wu, T.; Zhang, J.; Zhao, P. Study on the Formation Mechanism of Hydrothermal Prefabricated Activated Carbon and Its Adsorption Capacity for Malachite Green. *Colloid Polym. Sci.* **2022**, *300*, 973–988. [[CrossRef](#)]
42. Ning, X.; Teng, H.; Wang, G.; Zhang, J.; Zhang, N.; Huang, C.; Wang, C. Physicochemical, Structural and Combustion Properties of Hydrochar Obtained by Hydrothermal Carbonization of Waste Polyvinyl Chloride. *Fuel* **2020**, *270*, 117526. [[CrossRef](#)]
43. Zhang, X.; Liu, S.; Wang, M.; Ma, X.; Sun, X.; Liu, X.; Wang, L.; Wang, W. Hydrochar Magnetic Adsorbent Derived from Chinese Medicine Industry Waste via One-Step Hydrothermal Route: Mechanism Analyses of Magnetism and Adsorption. *Fuel* **2022**, *326*, 125110. [[CrossRef](#)]
44. Oumabady, S.; Selvaraj, P.S.; Periasamy, K.; Veeraswamy, D.; Ramesh, P.T.; Palanisami, T.; Ramasamy, S.P. Kinetic and Isotherm Insights of Diclofenac Removal by Sludge Derived Hydrochar. *Sci. Rep.* **2022**, *12*, 2184. [[CrossRef](#)]
45. Mirsoleimani-Azizi, S.M.; Setoodeh, P.; Zeinali, S.; Rahimpour, M.R. Tetracycline Antibiotic Removal from Aqueous Solutions by MOF-5: Adsorption Isotherm, Kinetic and Thermodynamic Studies. *J. Environ. Chem. Eng.* **2018**, *6*, 6118–6130. [[CrossRef](#)]
46. Muttakin, M.; Mitra, S.; Thu, K.; Ito, K.; Saha, B.B. Theoretical Framework to Evaluate Minimum Desorption Temperature for IUPAC Classified Adsorption Isotherms. *Int. J. Heat Mass Transf.* **2018**, *122*, 795–805. [[CrossRef](#)]

47. Thommes, M.; Kaneko, K.; Neimark, A.V.; Olivier, J.P.; Rodriguez-Reinoso, F.; Rouquerol, J.; Sing, K.S.W. Physisorption of Gases, with Special Reference to the Evaluation of Surface Area and Pore Size Distribution (IUPAC Technical Report). *Pure Appl. Chem.* **2015**, *87*, 1051–1069. [[CrossRef](#)]
48. Zhang, S.; Sheng, K.; Yan, W.; Liu, J.; Shuang, E.; Yang, M.; Zhang, X. Bamboo Derived Hydrochar Microspheres Fabricated by Acid-Assisted Hydrothermal Carbonization. *Chemosphere* **2021**, *263*, 128093. [[CrossRef](#)]
49. Foo, K.Y.; Hameed, B.H. Insights into the Modeling of Adsorption Isotherm Systems. *Chem. Eng. J.* **2010**, *156*, 2–10. [[CrossRef](#)]
50. Walsh, K.; Mayer, S.; Rehmann, D.; Hofmann, T.; Glas, K. Equilibrium Data and Its Analysis with the Freundlich Model in the Adsorption of Arsenic(V) on Granular Ferric Hydroxide. *Sep. Purif. Technol.* **2020**, *243*, 116704. [[CrossRef](#)]
51. Tzabar, N.; ter Brake, H.J.M. Adsorption Isotherms and Sips Models of Nitrogen, Methane, Ethane, and Propane on Commercial Activated Carbons and Polyvinylidene Chloride. *Adsorption* **2016**, *22*, 901–914. [[CrossRef](#)]
52. Ayawei, N.; Ebelegi, A.N.; Wankasi, D. Modelling and Interpretation of Adsorption Isotherms. *J. Chem.* **2017**, *2017*, 3039817. [[CrossRef](#)]
53. Humans, I.W.G. on the E. of C.R. to Mercury and Mercury Compounds. *IARC Monogr. Eval. Carcinog. Risks Hum.* **1993**, *58*, 239–345.
54. Coetzee, J.F.; Campion, J.J.; Liberman, D.R. Reactions of Silver(I), Mercury(I), and Mercury(II) with Halide Ions in Acetonitrile as Solvent. *Anal. Chem.* **1973**, *45*, 343–347. [[CrossRef](#)]
55. Jorgetto, A.D.O.; Da Silva, A.C.P.; Wondracek, M.H.P.; Silva, R.I.V.; Velini, E.D.; Saeki, M.J.; Pedrosa, V.A.; Castro, G.R. Multilayer Adsorption of Cu(II) and Cd(II) over Brazilian Orchid Tree (Pata-de-Vaca) and Its Adsorptive Properties. *Appl. Surf. Sci.* **2015**, *345*, 81–89. [[CrossRef](#)]
56. Imla Syafiqah, M.S.; Yussof, H.W. Kinetics, Isotherms, and Thermodynamic Studies on the Adsorption of Mercury (II) Ion from Aqueous Solution Using Modified Palm Oil Fuel Ash. *Mater. Today Proc.* **2018**, *5*, 21690–21697. [[CrossRef](#)]
57. Mapombere, G.; Nyoni, B.; Sibali, L.L.; Chiririwa, H.; Seodigeng, T. Tumisang Adsorption of Mercury by Pterocarpus Anglensis: Study on Adsorption Isotherms and Kinetics. *J. Chem. Chem. Eng. Res. Artic.* **2022**, *41*, 143–153.
58. Mohammadnia, E.; Hadavifar, M.; Veisi, H. Kinetics and Thermodynamics of Mercury Adsorption onto Thiolated Graphene Oxide Nanoparticles. *Polyhedron* **2019**, *173*, 114139. [[CrossRef](#)]
59. Huang, Y.; Lee, X.; Grattieri, M.; Macazo, F.C.; Cai, R.; Minter, S.D. A Sustainable Adsorbent for Phosphate Removal: Modifying Multi-Walled Carbon Nanotubes with Chitosan. *J. Mater. Sci.* **2018**, *53*, 12641–12649. [[CrossRef](#)]
60. Lu, J.; Xu, K.; Yang, J.; Hao, Y.; Cheng, F. Nano Iron Oxide Impregnated in Chitosan Bead as a Highly Efficient Sorbent for Cr(VI) Removal from Water. *Carbohydr. Polym.* **2017**, *173*, 28–36. [[CrossRef](#)]
61. López-Luna, J.; Ramírez-Montes, L.E.; Martínez-Vargas, S.; Martínez, A.I.; Mijangos-Ricardez, O.F.; del Carmen A. González-Chávez, M.; Carrillo-González, R.; Solís-Domínguez, F.A.; del Carmen Cuevas-Díaz, M.; Vázquez-Hipólito, V. Linear and Nonlinear Kinetic and Isotherm Adsorption Models for Arsenic Removal by Manganese Ferrite Nanoparticles. *SN Appl. Sci.* **2019**, *1*, 950. [[CrossRef](#)]
62. Pan, Y.; Shi, X.; Cai, P.; Guo, T.; Tong, Z.; Xiao, H. Dye Removal from Single and Binary Systems Using Gel-like Bioadsorbent Based on Functional-Modified Cellulose. *Cellulose* **2018**, *25*, 2559–2575. [[CrossRef](#)]
63. Li, Y.; Tsend, N.; Li, T.K.; Liu, H.; Yang, R.; Gai, X.; Wang, H.; Shan, S. Microwave Assisted Hydrothermal Preparation of Rice Straw Hydrochars for Adsorption of Organics and Heavy Metals. *Bioresour. Technol.* **2019**, *273*, 136–143. [[CrossRef](#)] [[PubMed](#)]
64. Kimbi Yaah, V.B.; Zbair, M.; Botelho de Oliveira, S.; Ojala, S. Hydrochar-Derived Adsorbent for the Removal of Diclofenac from Aqueous Solution. *Nanotechnol. Environ. Eng.* **2021**, *6*, 3. [[CrossRef](#)]
65. Li, H.Z.; Zhang, Y.N.; Guo, J.Z.; Lv, J.Q.; Huan, W.W.; Li, B. Preparation of Hydrochar with High Adsorption Performance for Methylene Blue by Co-Hydrothermal Carbonization of Polyvinyl Chloride and Bamboo. *Bioresour. Technol.* **2021**, *337*, 125442. [[CrossRef](#)] [[PubMed](#)]
66. Nadarajah, K.; Bandala, E.R.; Zhang, Z.; Mundree, S.; Goonetilleke, A. Removal of Heavy Metals from Water Using Engineered Hydrochar: Kinetics and Mechanistic Approach. *J. Water Process Eng.* **2021**, *40*, 101929. [[CrossRef](#)]
67. Dhaouadi, F.; Sellaoui, L.; Hernández-Hernández, L.E.; Bonilla-Petriciolet, A.; Mendoza-Castillo, D.I.; Reynel-Ávila, H.E.; González-Ponce, H.A.; Taamalli, S.; Louis, F.; Lamine, A. Ben Preparation of an Avocado Seed Hydrochar and Its Application as Heavy Metal Adsorbent: Properties and Advanced Statistical Physics Modeling. *Chem. Eng. J.* **2021**, *419*, 129472. [[CrossRef](#)]
68. He, X.; Zhang, T.; Xue, Q.; Zhou, Y.; Wang, H.; Bolan, N.S.; Jiang, R.; Tsang, D.C.W. Enhanced Adsorption of Cu(II) and Zn(II) from Aqueous Solution by Polyethyleneimine Modified Straw Hydrochar. *Sci. Total Environ.* **2021**, *778*, 146116. [[CrossRef](#)]
69. Ghasemi, S.S.; Hadavifar, M.; Maleki, B.; Mohammadnia, E. Adsorption of Mercury Ions from Synthetic Aqueous Solution Using Polydopamine Decorated SWCNTs. *J. Water Process Eng.* **2019**, *32*, 100965. [[CrossRef](#)]
70. Hadavifar, M.; Bahramifar, N.; Younesi, H.; Li, Q. Adsorption of Mercury Ions from Synthetic and Real Wastewater Aqueous Solution by Functionalized Multi-Walled Carbon Nanotube with Both Amino and Thiolated Groups. *Chem. Eng. J.* **2014**, *237*, 217–228. [[CrossRef](#)]